Available online at www.sciencedirect.com
ScienceDirect
Journal of Computational Physics 225 (2007) 2283–2300
JOURNAL OF COMPUTATIONAL PHYSICS
www.elsevier.com/locate/jcp

3D simulations of early blood vessel formation

F. Cavalli [a], A. Gamba [b], G. Naldi [a,*], M. Semplice [a], D. Valdembri [c], G. Serini [c]

[a] *Dipartimento di Matematica, Università degli Studi di Milano, via Saldini 50, 20133 Milano, Italy*
[b] *Dipartimento di Matematica, Politecnico di Torino, Corso Duca degli Abruzzi 24, 10129, Torino, and INFN, unità di Torino, via P. Giura 1, 10125 Torino, Italy*
[c] *Department of Oncological Sciences and Division of Molecular Angiogenesis, Institute for Cancer Research and Treatment, University of Torino School of Medicine, Strada Provinciale 142 Km 3.95, 10060 Candiolo (TO), Italy*

Received 4 August 2006; received in revised form 22 January 2007; accepted 20 March 2007
Available online 11 April 2007

Abstract

Blood vessel networks form by spontaneous aggregation of individual cells migrating toward vascularization sites (vasculogenesis). A successful theoretical model of two-dimensional experimental vasculogenesis has been recently proposed, showing the relevance of percolation concepts and of cell cross-talk (chemotactic autocrine loop) to the understanding of this self-aggregation process. Here we study the natural 3D extension of the computational model proposed earlier, which is relevant for the investigation of the genuinely three-dimensional process of vasculogenesis in vertebrate embryos. The computational model is based on a multidimensional Burgers equation coupled with a reaction diffusion equation for a chemotactic factor and a mass conservation law. The numerical approximation of the computational model is obtained by high order relaxed schemes. Space and time discretization are performed by using TVD schemes and, respectively, IMEX schemes. Due to the computational costs of realistic simulations, we have implemented the numerical algorithm on a cluster for parallel computation. Starting from initial conditions mimicking the experimentally observed ones, numerical simulations produce network-like structures qualitatively similar to those observed in the early stages of *in vivo* vasculogenesis. We develop the computation of critical percolative indices as a robust measure of the network geometry as a first step towards the comparison of computational and experimental data.

Keywords: Relaxed schemes; Computational biology; Vasculogenesis simulations; IMEX schemes; Percolative analysis

1. Introduction

In recent years, biologists have collected many qualitative and quantitative data on the behavior of microscopic components of living beings. We are, however, still far from understanding in detail how these microscopic components interact to build functions which are essential for life. A problem of particular interest

* Corresponding author. Tel.: +39 02 50316134; fax: +39 02 50316090.
E-mail addresses: cavalli@mat.unimi.it (F. Cavalli), andrea.gamba@polito.it (A. Gamba), naldi@mat.unimi.it (G. Naldi), semplice@mat.unimi.it (M. Semplice), guido.serini@ircc.it (G. Serini).

0021-9991/$ - see front matter © 2007 Elsevier Inc. All rights reserved.
doi:10.1016/j.jcp.2007.03.030

which has been extensively investigated is the formation of patterns in biological tissues [2]. Such patterns often show self-similarity and scaling laws [18] similar to those emerging in the physics of phase transitions [26].

The vascular network [28,29] is a typical example of a natural structure characterized by non-trivial scaling laws. In recent years many experimental investigations have been performed on the mechanism of blood vessel formation [6] both in living beings and in *in vitro* experiments. Vascular networks form by spontaneous aggregation of individual cells traveling toward vascularization sites (vasculogenesis). A successful theoretical model of two-dimensional experimental vasculogenesis has been recently proposed, showing the relevance of percolation concepts and of cell cross-talk (chemotactic autocrine loop) to the understanding of this self-aggregation process.

Theoretical and computational modelling is useful in testing biological hypotheses in order to explain which kind of coordinated dynamics gives origin to the observed highly structured tissue patterns. One can develop computational models based on simple dynamical principles and test whether they are able to reproduce the experimentally observed features. If the basic dynamical principles are correctly chosen, computational experiments allow to observe the emergence of complex structures from a multiplicity of interactions following simple rules.

Apart from the purely theoretical interest, reproducing biological dynamics by computational models allows to identify biochemical and biophysical parameters which are the most important in driving the process. This way, computational models can produce a deeper understanding of biological mechanisms, which in principle may end up having relevant practical consequences. It is worth noticing here that a complete understanding of the vascularization process is possible only if it is considered in its natural three-dimensional setting [1,7].

In this paper we illustrate computational results regarding the simulation of vascular network formation in a three-dimensional environment. We consider the three-dimensional version of the model proposed in [10,23]. The model is based on a Burgers-like equation, a well studied paradigm in the theory of pattern formation, integrated with a feedback term describing the chemotactic autocrine loop. The numerical evolution of the computational model, starting from initial conditions mimicking the experimentally observed ones, produces network-like structures qualitatively similar to those observed in the early stages of *in vivo* vasculogenesis.

Since in the long run we are interested in developing a quantitative comparison between experimental data and theoretical model, we start by selecting a set of observable quantities providing robust quantitative information on the network geometry. The lesson learned from the study of two-dimensional vasculogenesis is that percolative exponents [27] are an interesting set of such observables, so we test the computation of percolative exponents on simulated network structures.

A thorough quantitative comparison of the geometrical properties of experimental and computational network structures will become possible as soon as an adequate amount of experimental data, allowing proper statistical computation, will become available.

The paper is organized as follows: Section 2 summarizes some background knowledge on the biological problem of vascular network formation. Section 3 is a short review of the properties of the model introduced in [10,23]. In Section 4 the numerical approximation technique for the model is described. In Section 5 we describe the qualitative properties of simulated network structures and present the results of the computation of the exponents of the percolative transition. Finally, in the Conclusions, we point out predictable developments of our research.

2. Biological background

To supply tissues with nutrients in an optimal way, vertebrates have developed a hierarchical vascular system which terminates in a network of size-invariant units, i.e. capillaries. Capillary networks characterized by inter capillary distances ranging from 50 to 300 μm are essential for optimal metabolic exchange [11].

Capillaries are made of endothelial cells. Their growth is essentially driven by two processes: vasculogenesis and angiogenesis [6]. Vasculogenesis consists of local differentiation of precursor cells to endothelial ones, that assemble into a vascular network by directed migration and cohesion. Angiogenesis is essentially characterized by sprouting of novel structures and their remodelling.

In two-dimensional assays, the process of formation of a vascular network starting from randomly seeded cells can be accurately tracked by video microscopy [10] and it is observed to proceed along three main stages: (i) migration and early network formation, (ii) network remodelling and (iii) differentiation in tubular structures. During the first phase, which is the most important for determining the final geometrical properties of the structures, cells migrate over distances which are an order of magnitude larger than their radius and aggregate when they adhere with one of their neighbours. An accurate statistics of individual cells trajectories has been presented in [10], showing that, in the first stage of the dynamics, cell motion has marked directional persistence, pointing toward zones of higher cell concentration. This indicates that cells communicate through the emission of soluble chemical factors that diffuse (and degrade) in the surrounding medium, moving toward the gradients of this chemical field. Cells behave like indirectly interacting particles, the interaction being mediated by the release of soluble chemotactic factors. Their dynamics is well reproduced by the theoretical model proposed in [10].

The lessons learned from the study of in vitro vasculogenesis is thus that the formation of experimentally observed structures can be explained as the consequence of cell motility and of cell cross-talk mediated by the exchange of soluble chemical factors (chemotactic autocrine loop). The theoretical model also shows that the main factors determining the qualitative properties of the observed vascular structures are the available cell density and the diffusivity and half-life of the soluble chemoattractant. It seems that only the dynamical rules followed by the individual cell are actually encoded in the genes. The interplay of these simple dynamical rules with the geometrical and physical properties of the environment produces the highly structured final result.

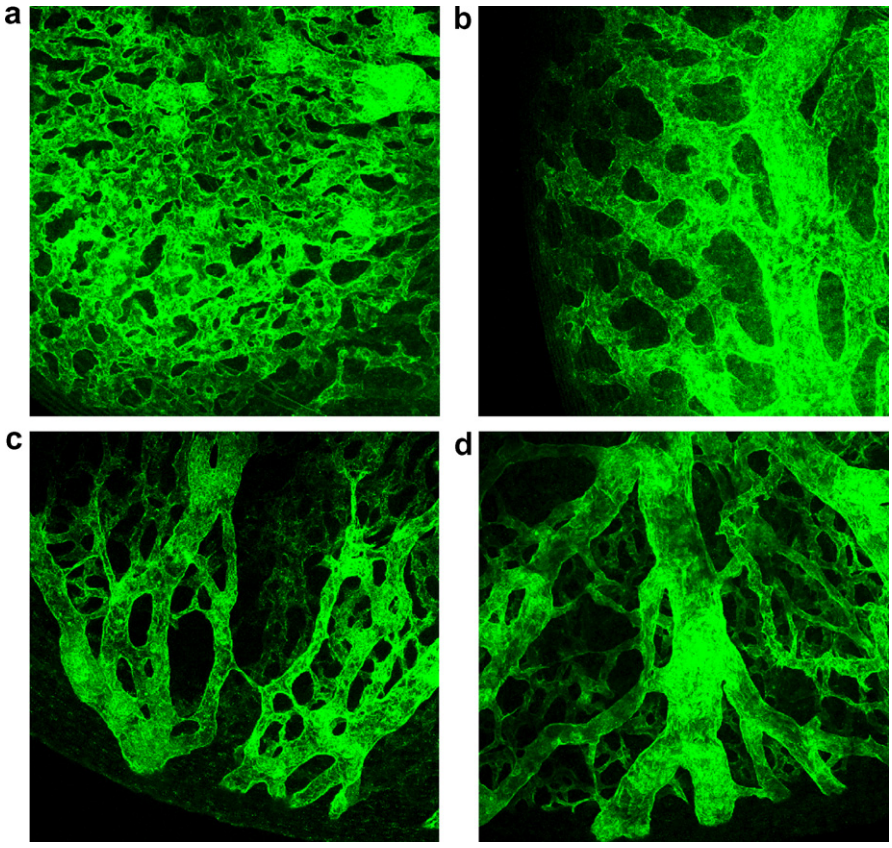

Fig. 1. Vascular networks formed by vasculogenesis in chick embryo brain, at various stages of development, classified according to Hamilton and Hamburger (HH). (a) HH stage 17, corresponding to 52–64 h; (b) HH stage 20 (70–72 h); (c and d) HH stage 26 (5 days).

At the moment, no direct observation of the chemotactic autocrine loop regulating vascular network formation is available, although several indirect biochemical observations point to it, so, the main evidence in this sense still comes from the theoretical analysis of computational models.

Today several major developments in three-dimensional cell culture and in cell and tissue imaging allow the observation of the mechanisms of cell migration and aggregation in three-dimensional settings in real time [9,21].

In the embryo, endothelial cells are produced and migrate in a three-dimensional scaffold, the extracellular matrix. Migration is actually performed through a series of biochemical processes, such as sensing of chemotactic gradients, and of mechanical operations, such as extensions, contractions, and degradation of the extracellular matrix along the way.

The evidence provided by two-dimensional experimental vasculogenesis suggests that cell motion can be directed by an autocrine loop of soluble chemoattractant factors also in the real three-dimensional environment.

As a sample of typical vascular structures that are observed in a three-dimensional setting in the early stages of development of a living being, we include here $(750\ \mu m)^2$ images of chick embryo brain at different development stages (Fig. 1). At an early stage (about 52–64 h) one observes a typical immature vascular network formed by vasculogenesis and characterized by a high density of similar blood vessels (Fig. 1a). At the next stage (70–72 h) we observe initial remodelling of the vascular network (Fig. 1b and c). Remodelling becomes more evident when the embryo is 5 days old, when blood vessels are organized in a mature, hierarchically organized vascular tree (Fig. 1d).

The mathematical model described in this paper is about the formation of an early network (like the one in Fig. 1a). The other pictures are shown to illustrate the successive development towards a hierarchical fully functional vascular network. In any case, a good prediction of the formation of the early vascular network is essential for understanding the subsequent remodelling.

3. Mathematical model of blood vessel growth

The multidimensional Burgers' equation is a well-known paradigm in the study of pattern formation. It gives a coarse grained hydrodynamic description of the motion of independent agents performing rectilinear motion and interacting only at very short ranges. These equations have been utilized to describe the emergence of structured patterns in many different physical settings (see e.g. [24,15]). In the early stages of dynamics, each particle moves with a constant velocity, given by a random statistical distribution. This motion gives rise to intersection of trajectories and formation of shock waves. After the birth of these local singularities, regions of high density grow and form a peculiar network-like structure. The main feature of this structure is the existence of comparatively thin layers and filaments of high density that separate large low-density regions.

In order to study and identify the factors influencing blood vessel formation one has to take into account evidence suggesting that cells do not behave as independent agents, but rather exchange information in the form of soluble chemical factors. This leads to the model proposed by Gamba et al. [10] and Serini et al. [23]. The model describes the motion of a fluid of randomly seeded independent particles which communicate through emission and absorption of a soluble factor and move toward its concentration gradients.

3.1. Model equations

The cell population is described by a continuous density $n(\mathbf{x}, t)$, where $\mathbf{x} \in \mathbf{R}^d$ $(d = 2,3)$ is the space variable, and $t \geqslant 0$ is the time variable. The population density moves with velocities $\mathbf{v}(\mathbf{x}, t)$, that are stimulated by chemical gradients of a soluble factor. The chemoattractant soluble factor is described by a scalar chemical concentration field $c(\mathbf{x}, t)$. It is supposed to be released by the cells, diffuse, and degrade in a finite time, in agreement with experimental observations.

The dynamics of the cell density can be described by coupling three equations. The first one is the mass conservation law for cell matter, which expresses the conservation of the number of cells. The second one is a momentum balance law that takes into account the phenomenological chemotactic force, the dissipation by interaction with the substrate, the phenomenon of cell directional persistency along their trajectories and a

term implementing an excluded volume constraint [10,3]. Finally there is a reaction-diffusion equation for the production, degradation and diffusion of the concentration of the chemotactic factor. One then has the following system:

$$\frac{\partial n}{\partial t} + \nabla \cdot (n\mathbf{v}) = 0 \tag{1a}$$

$$\frac{\partial \mathbf{v}}{\partial t} + \mathbf{v} \cdot \nabla \mathbf{v} = \mu(c)\nabla c - \nabla\phi(n) - \beta(c)\mathbf{v} \tag{1b}$$

$$\frac{\partial c}{\partial t} = D\Delta c + \alpha(c)n - \frac{c}{\tau} \tag{1c}$$

where μ measures the cell response to the chemotactic factor, while D and τ are respectively the diffusion coefficient and the characteristic degradation time of the soluble chemoattractant. The function α determines the rate of release of the chemical factor. The friction term $-\beta\mathbf{v}$ mimics the dissipative interaction of the cells with the extracellular matrix.

A simple model can be obtained by assuming that the cell sensitivity μ, the rate of release of the chemoattractant α and the friction coefficient β are constant. A more realistic description may be obtained including saturation effects as functional dependencies of the aforementioned coefficients on the concentration c. We point out that μ determines the time scale of the evolutionary process, i.e. the time elapsed before the stationary state is reached.

The term $\nabla\phi(n)$ is a density-dependent pressure term, where $\phi(n)$ is zero for low densities, and increases for densities above a suitable threshold. This pressure is a phenomenological term which models short range interaction between cells and the fact that cells do not interpenetrate.

We observe that, at low density n and for small chemoattractive gradients, (1b) is an inviscid Burgers' equation for the velocity field $\mathbf{v}$ [5], coupled to the standard reaction-diffusion equation (1c) and the mass conservation law (1a).

Since in the early stages of development almost all intraembryonic mesodermal tissues contain migrating endothelial precursors, we use initial conditions representing a randomly scattered distribution of cells, *i.e.*, we throw an assigned number of cells in random positions inside the cubic box, with zero initial velocities and zero initial concentration of the soluble factor, with a single cell given initially by a Gaussian bump of width σ of the order of the average cell radius ($\simeq$15 μm) and unitary weight in the integrated cell density field n.

In order to model the fact that closely packed cells resist to compression, a phenomenological, density dependent, pressure $\nabla\phi(n)$ acting only when cells become close enough to each other is introduced. The potential ϕ has to be monotonically increasing and constant for $n < n_0$ where n_0 is the close-packing density. For simplicity we choose the functional form

$$\phi(n) = \begin{cases} B_p(n - n_0)^{C_p} & n > n_0 \\ 0 & n \leqslant n_0 \end{cases} \tag{2}$$

3.2. Parameter values

Fourier analysis of Eq. (1c) with constant parameters and in the fast diffusion approximation $\partial c/\partial t = 0$ suggests that starting from the aforementioned initial conditions, system (1) should develop network patterns characterized by a typical length scale $r_0 = \sqrt{D\tau}$, which is the effective range of the interaction mediated by soluble factors. As a matter of fact, Fourier components $\hat{c}_k$ of the chemical field are related to the Fourier components of the density field $\hat{n}_k$ by the relation

$$\hat{c}_k = \frac{\alpha\tau\hat{n}_k}{D\tau k^2 + 1}.$$

This means that in system (1) wavelengths of the field n of order r_0 are amplified, while wavelengths $\lambda \gg r_0$ or $\lambda \ll r_0$ are suppressed.

Initial conditions introduce in the problem a typical length scale given by the average cell–cell distance $L/\sqrt{N}$, where L is the system size and N the particle number. The dynamics, filtering wavelengths [8], rearranges the matter and forms a network characterized by the typical length scale r_0.

It is interesting to check the compatibility of the theoretical prediction with physical data. From available experimental results [22] it is known that the order of magnitude of the diffusion coefficient for major angiogenic growth factors is $D = 10^{-7}\ \mathrm{cm^2\ s^{-1}}$. In the experimental conditions that were considered in [10] the half-life of soluble factors is 64 ± 7 min. This gives $r_0 \sim 200\ \mu\mathrm{m}$, a value in good agreement with experimental observations.

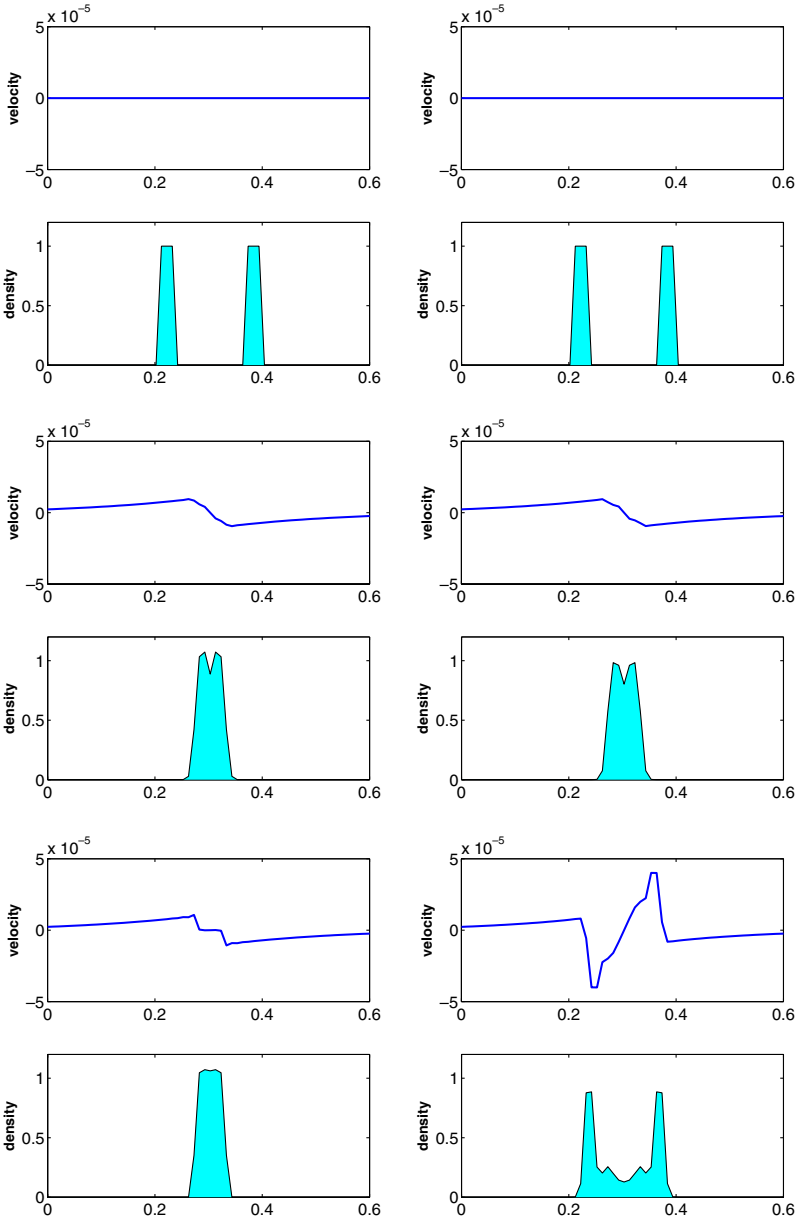

Fig. 2. Bump coalescence driven by chemotactic force and pressure. The density and velocity fields at subsequent instants of time are shown. Left column: $C_p = 3$ and $B_p = 10^{-3}$, leading to bump coalescence. Right column: $C_p = 2$ and $B_p = 10^{-1}$, leading to undesired rebound of the two bumps.

3.3. Lower dimensional models

In order to get some intuition about the typical system dynamics, we exploit the 1D version of model (1) to simulate the "collision" of two cells. We verified numerically that for $B_p < 10^{-2}$ and $C_p > 2.5$ in (2), the two bumps merge into a single one (see Fig. 2 left) which appears to be stationary, as suggested also by the graphs of the kinetic energy and of the momentum of inertia (Fig. 3 top). On the other hand a less smooth onset of pressure obtained with larger B_p or smaller C_p leads to forces overcoming the chemical attractive ones, making the two bumps bounce back (Fig. 2 right, Fig. 3 bottom). We observe that the dynamics that better reproduces the biological behavior is the one where the two bumps coalesce.

Biological observations suggest that the dynamics of cell changes when they establish cell–cell contacts. It is reasonable to suppose that a different genetic program is activated at this moment, disabling cell motility. We therefore switch off cell motility as soon as the cell concentration, signalled by chemoattractant emission, reaches a given threshold. In this way the computational system is guaranteed to reach a stationary state.

These effects can be taken into account using a non-constant sensitivity $\mu(c)$, a non-linear emission rate $\alpha(c)$, or a variable friction coefficient $\beta(c)$. We choose a threshold c_0 and functions of the form

$$\mu(c) = \mu_0[1 - \tanh(c - c_0)] \tag{3a}$$

$$\alpha(c) = \alpha_0[1 - \tanh(c - c_0)] \tag{3b}$$

$$\beta(c) = \beta_0[1 + \tanh(c - c_0)] \tag{3c}$$

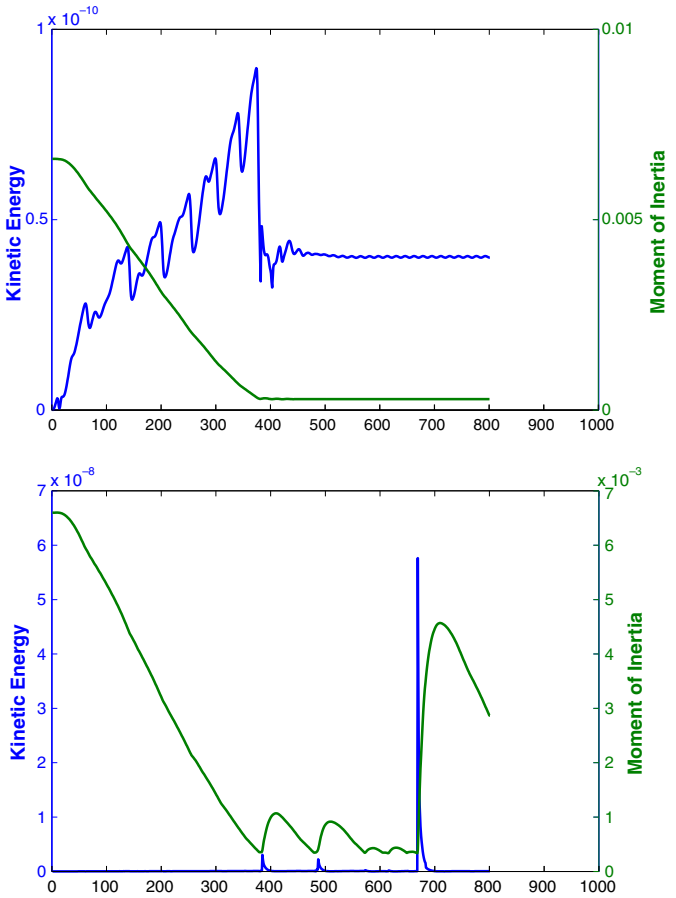

Fig. 3. Time evolution of the kinetic energy (solid line) and of the momentum of inertia (dashed line). Top: $C_p = 3$ and $B_p = 10^{-3}$, leading to bump coalescence. Bottom: $C_p = 2$ and $B_p = 10^{-1}$, leading to undesired rebound of the two bumps.

The effect of the first two terms is that the sensitivity of the cells and their chemoattractant production is strongly damped when the concentration c reaches the threshold c_0. We did not observe a significant dependence on the exact form of the damping function, provided that it approximates a step function that is nonzero only when $c < c_0$.

$\beta(c)$, on the other hand has the effect of turning on a strong friction term at locations of high chemoattractant concentration. We performed several tests and observed that the different choices (3) are approximately equivalent in freezing the system into a network-like stationary state.

4. Numerical methods

Our numerical scheme is based on a suitable relaxation approximation [13] of the mass conservation law (1a) and the multidimensional Burgers equation (1b) coupled with a second order finite-differences method for the reaction-diffusion equation (1c) of the chemotactic factor. We point out that also for the last Eq. (1c) we could consider a relaxation approximation [14,19] in order to deal with the system (1) in an uniform way, but we prefer to adopt here a simpler approach.

We first briefly review an extension of the approach proposed by Jin and Xin in [13] for a scalar conservation law to the case when a source term is present

$$\frac{\partial u}{\partial t} + \frac{\partial}{\partial x} f(u) = g(u). \tag{4}$$

Introducing an auxiliary variable j that plays the role of a physical flux we consider the following relaxation system:

$$\frac{\partial u}{\partial t} + \frac{\partial j}{\partial x} = g(u) \tag{5a}$$

$$\frac{\partial j}{\partial t} + a\frac{\partial u}{\partial x} = -\frac{1}{\epsilon}(j - f(u)), \tag{5b}$$

where ϵ is a small positive parameter, called relaxation time, and a is a suitable positive constant. Formally, Chapman–Enskog expansion justifies the agreement of the solutions of the relaxation system with the solutions of the equation

$$\frac{\partial u}{\partial t} + \frac{\partial}{\partial x} f(u) = g(u) + \epsilon \frac{\partial}{\partial x}\left((a - f'(u)^2)\frac{\partial u}{\partial x}\right), \tag{6}$$

which is a first order approximation of the original balance law (4).

It is also clear that (6) is dissipative, provided that the subcharacteristic condition $a > f'(u)^2$ is satisfied. We would expect that appropriate numerical discretization of the relaxation system (5) yields accurate approximation to the original Eq. (4) when the relaxation parameter ϵ is sufficiently small.

In view of its numerical approximation, the main advantage of the relaxation system (5) over the original equation (4) lies in the linear structure of the characteristic fields and in the localized low order term and this avoids the use of time consuming Riemann solvers. Moreover, proper implicit time discretization can be exploited to overcome the stability constraints due to the stiffness and to avoid the use of non-linear solvers.

We observe that system (5) is in the form

$$\frac{\partial z}{\partial t} + \operatorname{div} f(z) = g(z) + \frac{1}{\epsilon} h(z), \tag{7}$$

where $z = (u, j)^{\mathrm{T}}, f(z) = (j, au)^{\mathrm{T}}, g(z) = (g(u), 0)^{\mathrm{T}}$ and $h(z) = (0, j - f(u))^{\mathrm{T}}$. When ε is small, the presence of both non-stiff and stiff terms, suggests the use of IMEX schemes [4,16,20].

Assume for simplicity to adopt a uniform time step Δt and denote with z^n the numerical approximation at time $t_n = n\Delta t$, for $n = 0, 1, \ldots$ In our case a ν-stages IMEX scheme reads

$$z^{n+1} = z^n - \Delta t \sum_{i=1}^{\nu} \tilde{b}_i \left[\frac{\partial f}{\partial x}(z^{(i)}) + g(z^{(i)})\right] + \frac{\Delta t}{\varepsilon} \sum_{i=1}^{\nu} b_i h(z^{(i)}),$$

where the stage values are computed as

$$z^{(i)} = z^n - \Delta t \sum_{k=1}^{i-1} \tilde{a}_{i,k} \left[\frac{\partial f}{\partial x}(z^{(k)}) + g(z^{(k)}) \right] + \frac{\Delta t}{\varepsilon} \sum_{k=1}^{i} a_{i,k} h(z^{(k)})$$

Here (a_{ik}, b_i) and $(\tilde{a}_{ik}, \tilde{b}_i)$ are a pair of Butcher's tableaux of, respectively, a diagonally implicit and an explicit Runge–Kutta schemes.

In this work we use the so-called relaxed schemes that are obtained letting $\varepsilon \to 0$ in the numerical scheme for (7). For these, the first stage

$$\begin{bmatrix} u^{(1)} \\ j^{(1)} \end{bmatrix} = \begin{bmatrix} u^n \\ j^n \end{bmatrix} + \frac{\Delta t}{\varepsilon} a_{1,1} h\left(\begin{bmatrix} u^{(1)} \\ j^{(1)} \end{bmatrix} \right)$$

becomes

$$u^{(1)} = u^n \quad j^{(1)} = f(u^{(1)}),$$

then it reduces to $h(z^{(1)}) = 0$. The second stage, $i = 2$, now reads

$$z^{(2)} = z^n - \Delta t \tilde{a}_{2,1} \left[\frac{\partial f}{\partial x}(z^{(1)}) + g(z^{(1)}) \right] + \frac{\Delta t}{\varepsilon} a_{2,1} \underbrace{h(z^{(1)})}_{\equiv 0} + \frac{\Delta t}{\varepsilon} a_{2,2} h(z^{(2)})$$

which implies that $h(z^{(2)}) = 0$.

Summarizing, the relaxed scheme yields an alternation of relaxation steps

$$h(z^{(i)}) = 0 \quad \text{i.e.} \quad j^{(i)} = f(u^{(i)})$$

and transport steps where we advance for time $\tilde{a}_{i,k} \Delta t$

$$\frac{\partial z}{\partial t} + \operatorname{div} f(z) = g(z)$$

with initial data $z = z^{(i)}$ retain only the first component and assign it to $u^{(i+1)}$.

Finally the value of u^{n+1} is computed as $u^n + \sum \tilde{b}_i u^{(i)}$.

In order to obtain a relaxation approximation of the first and second equation of (1) we rewrite them in conservative form, introducing the moment $\mathbf{p}(\mathbf{x}, t) = n(\mathbf{x}, t)\mathbf{v}(\mathbf{x}, t)$:

$$\frac{\partial n}{\partial t} + \nabla \cdot \mathbf{p} = 0 \tag{8a}$$

$$\frac{\partial \mathbf{p}}{\partial t} + \nabla \cdot (n\mathbf{v} \otimes \mathbf{v}) = n\mu \nabla c - n \nabla \phi(n) - \beta \mathbf{p} \tag{8b}$$

Introducing the variable $\mathbf{u} = (n, \mathbf{p})^{\mathrm{T}}$ and the auxiliary flux $\mathbf{w}$, the relaxation system reads

$$\frac{\partial \mathbf{u}}{\partial t} + \nabla \cdot \mathbf{w} = G(\mathbf{u}, \mathbf{w}, c) \tag{9a}$$

$$\frac{\partial \mathbf{w}}{\partial t} + A \nabla \cdot \mathbf{u} = -\frac{1}{\varepsilon}(\mathbf{w} - F(\mathbf{u})) \tag{9b}$$

where $G(\mathbf{u}, \mathbf{w}, c) = (0, n\mu \nabla c - n \nabla \phi(n) - \beta \mathbf{p})^{\mathrm{T}}$, $F(\mathbf{u}) = (\mathbf{p}, n\mathbf{v} \otimes \mathbf{v})$ and A is a suitable diagonal matrix whose positive diagonal elements verify a subcharacteristic condition [13] in order to ensure the dissipativity of the relaxation system.

For a one-dimensional scalar conservation law $u_t + f(u)_x = 0$, A is a scalar and such condition reads $A \geqslant |f'(u)|^2$ [13]. In the present case, it is sufficient that the entries of the diagonal matrix A be greater or equal than the eigenvalues of the Jacobian of the flux F, which for system (9) are the three components of the velocity $\mathbf{v}$. Hence we choose $A_{ii} = \max(v_i)$ at each time step, in order to reduce the numerical diffusion, which arises when the choice of A is non-optimal, see [13].

As we previously remarked, our relaxed scheme takes alternatively an implicit step and an explicit one: the explicit step involves the computation of the flux $\nabla \cdot \mathbf{w}$ and the evaluation of the non-stiff source term G. In particular we compute ∇c and $\nabla \phi(n)$ using a second order centered difference scheme.

In the following we describe for simplicity the fully discrete scheme in one-dimensional case. We introduce the spatial grid points x_j with uniform mesh width $h = x_{j+1} - x_j$. As usual, we denote by u_j^n the approximate cell average of a quantity u in the cell $[x_{j-1/2}, x_{j+1/2}]$ at time t_n and by $u_{j+1/2}^n$ the approximate point value of u at $x = x_{j+1/2}$ and $t = t_n$. A spatial discretization to (9) in conservation form can be written as

$$\frac{\partial \mathbf{u}_j}{\partial t} + \frac{1}{h}(\mathbf{w}_{j+1/2} - \mathbf{w}_{j-1/2}) = G(\mathbf{u}_j, \mathbf{w}_j, c_j) \tag{10a}$$

$$\frac{\partial \mathbf{w}_j}{\partial t} + \frac{1}{h}A(\mathbf{u}_{j+1/2} - \mathbf{u}_{j-1/2}) = -\frac{1}{\varepsilon}(\mathbf{w}_j - F(\mathbf{u}_j)). \tag{10b}$$

In order to compute the numerical fluxes $\mathbf{w}_{j\pm1/2}$, we consider the characteristic variables $\mathbf{w} \pm A^{1/2}\mathbf{u}$ that travel with constant velocities $\pm A^{1/2}$, and so the semidiscrete system becomes diagonal. Now we have to apply a numerical approximation to $\mathbf{w} \pm A^{1/2}\mathbf{u}$. A first idea could be to apply a ENO or WENO approach (see e.g. [25]), to build an high order reconstruction, coupled with a suitable IMEX scheme. The drawback is the high computational costs, especially in a multidimensional framework. Therefore we chose a suitable compromise between the computational cost and the accuracy, using a second order TVD scheme. The numerical flux that we use is obtained coupling an upwind scheme and the Lax–Wendroff method by a non-linear flux limiter [17]. Namely the high order flux $F(\mathrm{U})$ for a generic variable U consists of the low order term $F_{\mathrm{L}}(U)$ plus a second order correction $F_{\mathrm{H}}(U)$:

$$F(U) = F_{\mathrm{L}}(U) + \Psi(U)(F_{\mathrm{H}}(U) - F_{\mathrm{L}}(U))$$

where Ψ is the flux limiter. When the data U is smooth, then $\Psi(U)$ should be near 1, while near a discontinuity we want $\Psi(U)$ close to 0. The idea consists in the selection of a high order flux F_{H} that works well in smooth regions and of a low order flux F_{L} which behaves well near discontinuities.

In our schemes we considered the upwind scheme as a low order flux for the characteristic variables

$$F_{\mathrm{L}}((\mathbf{w} + A^{1/2}\mathbf{u})_{j+1/2}) = (\mathbf{w} + A^{1/2}\mathbf{u})_j, \quad F_{\mathrm{L}}((\mathbf{w} - A^{1/2}\mathbf{u})_{j+1/2}) = (\mathbf{w} - A^{1/2}\mathbf{u})_{j+1}$$

and the Lax–Wendroff scheme as a high order flux for the same variables

$$F_{\mathrm{H}}((\mathbf{w} \pm A^{1/2}\mathbf{u})_{j+1/2}) = \frac{A^{1/2}}{2}((\mathbf{w} \pm A^{1/2}\mathbf{u})_{j+1} + (\mathbf{w} \pm A^{1/2}\mathbf{u})_j) - \frac{\lambda A^{1/2}}{2}((\mathbf{w} \pm A^{1/2}\mathbf{u})_{j+1} - (\mathbf{w} \pm A^{1/2}\mathbf{u})_j)$$

where $\lambda = \Delta t/h$ (we advance of one time step).

Letting

$$\mathbf{\Theta}_j^{\pm} = \left(\frac{(\mathbf{w} \pm A^{1/2}\mathbf{u})_j^n - (\mathbf{w} \pm A^{1/2}\mathbf{u})_{j-1}^n}{(\mathbf{w} \pm A^{1/2}\mathbf{u})_{j+1}^n - (\mathbf{w} \pm A^{1/2}\mathbf{u})_j^n}\right)^{\pm 1},$$

the fully discrete scheme for the variable $\mathbf{u}$ using Euler method to advance in time is the following

$$\mathbf{u}_j^{n+1} = \mathbf{u}_j^n + \frac{\lambda A^{1/2}}{2}(\mathbf{u}_{j+1}^n - 2\mathbf{u}_j^n + \mathbf{u}_{j-1}^n) - \frac{\lambda}{2}(\mathbf{w}_{j+1}^n - \mathbf{w}_{j-1}^n)\Delta t \frac{\mathrm{I} - \lambda A^{1/2}}{4}(-\mathbf{s}_j^+ + \mathbf{s}_{j-1}^+ + \mathbf{s}_{j+1}^- - \mathbf{s}_j^-),$$

with

$$\mathbf{s}_j^{\pm} = \frac{1}{h}(\pm A^{1/2}\mathbf{u}_{j\pm1}^n + \mathbf{w}_{j\pm1}^n \mp A^{1/2}\mathbf{u}_j^n - \mathbf{w}_j^n)\Psi(\Theta_j^{\pm}). \tag{11}$$

After the substitution of the relaxation step we get

$$\mathbf{u}_j^{n+1} = \mathbf{u}_j^n + \frac{\lambda A^{1/2}}{2}(\mathbf{u}_{j+1}^n - 2\mathbf{u}_j^n + \mathbf{u}_{j-1}^n) - \frac{\lambda}{2}(F(\mathbf{u}_{j+1}^n) - F(\mathbf{u}_{j+1}^n))\Delta t \frac{\mathrm{I} - \lambda A^{1/2}}{4}(-\mathbf{s}_j^+ + \mathbf{s}_{j-1}^+ + \mathbf{s}_{j+1}^- - \mathbf{s}_j^-),$$

where $\mathbf{s}^{\pm}$ is obtained from (11) letting $\mathbf{w} = F(\mathbf{u})$. The scheme can be put in a conservative form and it is possible to prove its consistency by standard technique [17]. In order to prove a TVD stability, we write

$$\mathbf{u}_{j+1}^{n+1} - \mathbf{u}_j^{n+1} = (1 - \mathbf{C}_j^n - \mathbf{D}_j^n)(\mathbf{u}_{j+1}^n - \mathbf{u}_j^n) + \mathbf{C}_{j-1}^n(\mathbf{u}_j^n - \mathbf{u}_{j-1}^n) + \mathbf{D}_{j+1}^n(\mathbf{u}_{j+2}^n - \mathbf{u}_{j+1}^n) + \mathbf{E}_{j+1/2}, \tag{12}$$

where

$$\mathbf{C}_j^n = \frac{\lambda}{2}\left(A^{1/2} + \frac{F(\mathbf{u}_{j+1}^n) - F(\mathbf{u}_j^n)}{\mathbf{u}_{j+1}^n - \mathbf{u}_j^n}\right)$$

$$\mathbf{D}_j^n = \frac{\lambda}{2}\left(A^{1/2} - \frac{F(\mathbf{u}_{j+1}^n) - F(\mathbf{u}_j^n)}{\mathbf{u}_{j+1}^n - \mathbf{u}_j^n}\right)$$

$$\mathbf{E}_{j+1/2}^n = \Delta t \frac{1 - \lambda A^{1/2}}{4}(\mathbf{s}_{j+2}^- - 2\mathbf{s}_{j+1}^- + \mathbf{s}_j^- - \mathbf{s}_{j+1}^+ + 2\mathbf{s}_j^+ - \mathbf{s}_{j-1}^+)$$

where we notice that $\mathbf{C}$ and $\mathbf{D}$ are non-negative.

The coefficient E can be written in terms of $\mathbf{C}$ and $\mathbf{D}$, in fact

$$\mathbf{s}_j^+ = \frac{2}{\lambda\Delta x}\mathbf{C}_i^n \Psi(\Theta_i^+)(\mathbf{u}_{j+1}^n - \mathbf{u}_j^n), \quad \mathbf{s}_j^- = -\frac{2}{\lambda\Delta x}\mathbf{D}_{i-1}^n \Psi(\Theta_i^-)(\mathbf{u}_j^n - \mathbf{u}_{j-1}^n).$$

We can rewrite (12) in the following form

$$\begin{aligned}\mathbf{u}_{j+1}^{n+1} - \mathbf{u}_j^{n+1} = {} & (\mathbf{u}_{j+1}^n - \mathbf{u}_j^n)[(1 - \mathbf{C}_j^n - \mathbf{D}_j^n) + (1 - \lambda A^{1/2})(\mathbf{D}_j^n \Psi_{j+1}^- + \mathbf{C}_j^n \Psi_j^+)] \\ & + (\mathbf{u}_j^n - \mathbf{u}_{j-1}^n)\left[\mathbf{C}_{j-1}^n - \frac{1 - \lambda A^{1/2}}{2}(\mathbf{D}_{j-1}^n \Psi_j^- + \mathbf{C}_{j-1}^n \Psi_{j-1}^+)\right] \\ & + (\mathbf{u}_{j+2}^n - \mathbf{u}_{j+1}^n)\left[\mathbf{D}_{j+1}^n - \frac{1 - \lambda A^{1/2}}{2}(\mathbf{D}_{j+1}^n \Psi_{j+2}^- + \mathbf{C}_{j+1}^n \Psi_{j+1}^+)\right]\end{aligned} \tag{13}$$

It's easy to see that under the CFL condition $\|\lambda\sqrt{\max\{a_i\}}\| \leqslant 1$, where a_i are the positive diagonal elements of the matrix A, and using the fact that the flux limiter verifies

$$0 \leqslant \frac{\Psi(\Theta)}{\Theta} \leqslant 2, \quad 0 \leqslant \Psi(\Theta) \leqslant 2,$$

we have

$$(1 - \mathbf{C}_j^n - \mathbf{D}_j^n) + (1 - \lambda A^{1/2})(\mathbf{D}_j^n \Psi_{j+1}^- + \mathbf{C}_j^n \Psi_j^+) \geqslant 0$$

$$\mathbf{C}_{j-1}^n - \frac{1 - \lambda A^{1/2}}{2}(\mathbf{D}_{j-1}^n \Psi_j^- + \mathbf{C}_{j-1}^n \Psi_{j-1}^+) \geqslant 0$$

$$\mathbf{D}_{j+1}^n - \frac{1 - \lambda A^{1/2}}{2}(\mathbf{D}_{j+1}^n \Psi_{j+2}^- + \mathbf{C}_{j+1}^n \Psi_{j+1}^+) \geqslant 0$$

and so we can deduce that our scheme is TVD stable from Harten's Theorem [12].

In the case of multidimensions, a similar discretization can be applied to each space dimension [13,14,19]. Then, since the structure of the multidimensional relaxation system is similar to the 1D system, the numerical implementation for higher dimensional problems, based on additive dimensional splitting, is not much harder than for 1D problems.

The time step Δt is chosen adaptively as follows. As explained above, the stability of the relaxed scheme for (8) requires that the CFL condition

$$\Delta t \leqslant \frac{h}{\max(a_i)} = \frac{h}{\max(v_i)}$$

be satisfied. On the other hand an explicit scheme for the diffusion operator would require a time step restriction of the form $\Delta t \leqslant h^2/6D$, where D is the diffusion coefficient, which is approximately $10^{-7}\,\mathrm{cm}^2\,\mathrm{s}^{-1}$ in our case. As the above condition becomes too restrictive when the mesh size is reduced (around $N > 100$ points per side), we employ the implicit Euler scheme for the diffusion equation and choose Δt at each time step accordingly to the hyperbolic CFL condition only.

In order to study the accuracy of the numerical scheme in the three-dimensional case, we analyzed the behavior of the error under mesh refinement. First we computed a reference solution by considering a mesh with 256^3 points, with 2900 cells and final time $t = 60$. We then interpolated the initial datum of the reference solution on grids with $64^3, 100^3, 128^3, 150^3, 180^3, 200^3$ points and performed the simulation with the same final time on these coarser grids. The final solution was compared with the reference one by computing the L^1 and L^2 norms of the error in the variable n. The errors and convergence rates are shown in Fig. 4.

For our three-dimensional problem the computational cost is quite high and can be reduced using parallel computing: the semilinearity of relaxation systems, together with our suitably chosen discretizations, provides parallel algorithm with almost optimal scaling properties. In particular the domain is divided in smaller subdomains and each subdomain is assigned to a processor. The computations of all non-linear terms involve only pointwise evaluations and it is easy to perform these tasks in a local way. Only point near the interfaces between different subdomain need to be communicated in the transport step. We implemented these algorithm on a high performance cluster for parallel computation installed at the Department of Mathematics of the University of Milano (http://cluster.mat.unimi.it/). The scaling properties of the algorithm are shown in

N	L^1		L^2	
64	1.1464e-01		3.7952e-04	
100	6.9761e-02	1.11	1.2647e-04	2.46
128	4.5696e-02	1.71	6.1748e-05	2.90
150	3.2725e-02	2.11	3.6507e-05	3.31
180	2.6910e-02	1.07	2.6667e-05	1.72
200	2.1930e-02	1.94	1.9818e-05	2.82

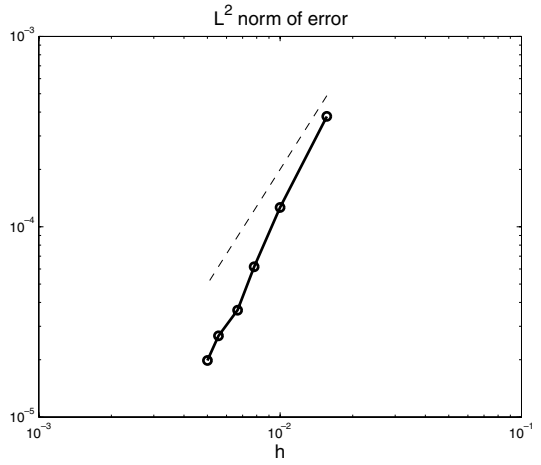

Fig. 4. Table of the L^2 and L^1 errors and convergence rates and graph of the L^2 errors with respect to the mesh size $h = 1/N$ (the dashed line corresponds to second order convergence rate).

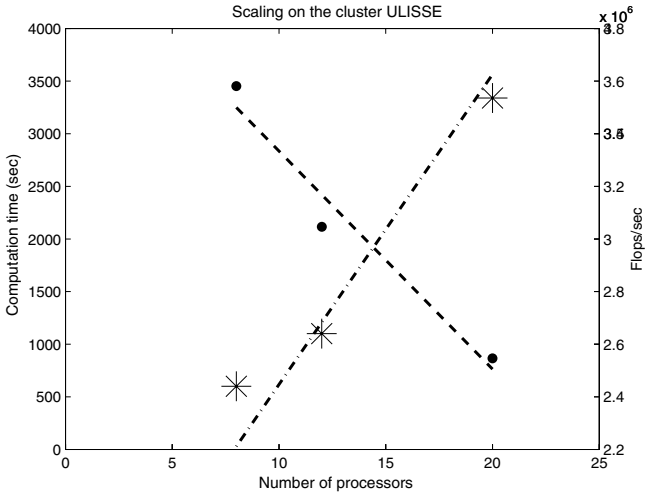

Fig. 5. Scaling of the 3D algorithm on the ULISSE cluster. Dots represent execution time(s) and asterisks the number of Mflops/s for our numerical algorithm. Dashed and dash-dot lines are linear least square approximations.

Fig. 5 and are essentially due to the exclusive use of matrix-vectors operations and to the avoidance of solvers for linear or non-linear systems.

5. Numerical results

We perform three-dimensional numerical simulations of model (1) on a cubic box with side of length $L = 1$ mm, with periodic boundary conditions. The initial condition is assigned in the form of a set of Gaussian bumps with $\sigma = 15$ μm scattered in the cube with uniform probability and having zero initial velocity.

Biochemical data [23] suggest the values $D = 10^{-7}$ cm^2 s^{-1} and $\tau = 4000$ s for the diffusion constant and the chemoattractant decay rate. We fix the other constant parameters by dimensional analysis and fitting to the characteristic scales of the biological system. In particular, we choose: $\mu_0 = 10^{-11}$ mm^4/s^3, $\alpha = 1$ s^{-1}, $\beta = 10^{-3}$ s^{-1}. For the coefficients in the expression (2) of the pressure function ϕ we take $n_0 = 1.0$, $C_p = 3$ and $B_p = 10^{-3}$.

Very fine grids have to be used in order to resolve the details of the $n(\mathbf{x}, t)$ field, which may contain hundreds of small bumps, each representing a single cell. Since each cell has radius $\sigma = 15$ μm, one needs a grid spacing such that $\Delta x < 10$ μm and therefore grids of at least 100^3 cells for a cubic domain of 1 mm side.

We performed numerical simulations with varying initial average cell density $\bar{n}$. We observed that the initially randomly distributed cells (Fig. 6) coalesce forming elongated structures (Fig. 7) and evolve towards a stationary state (Fig. 8) mimicking the geometry of a blood vessel network in the early stages of formation. The figures show an isosurface of the density variable n, together with two cross-section density plots.

We assigned $\bar{n}$ in the range 2100–3500 cells/mm^3 and performed 10–15 runs for each density value with a $128 \times 128 \times 128$ grid on a biological system of 1 mm^3. The characteristic lengths and geometrical properties of

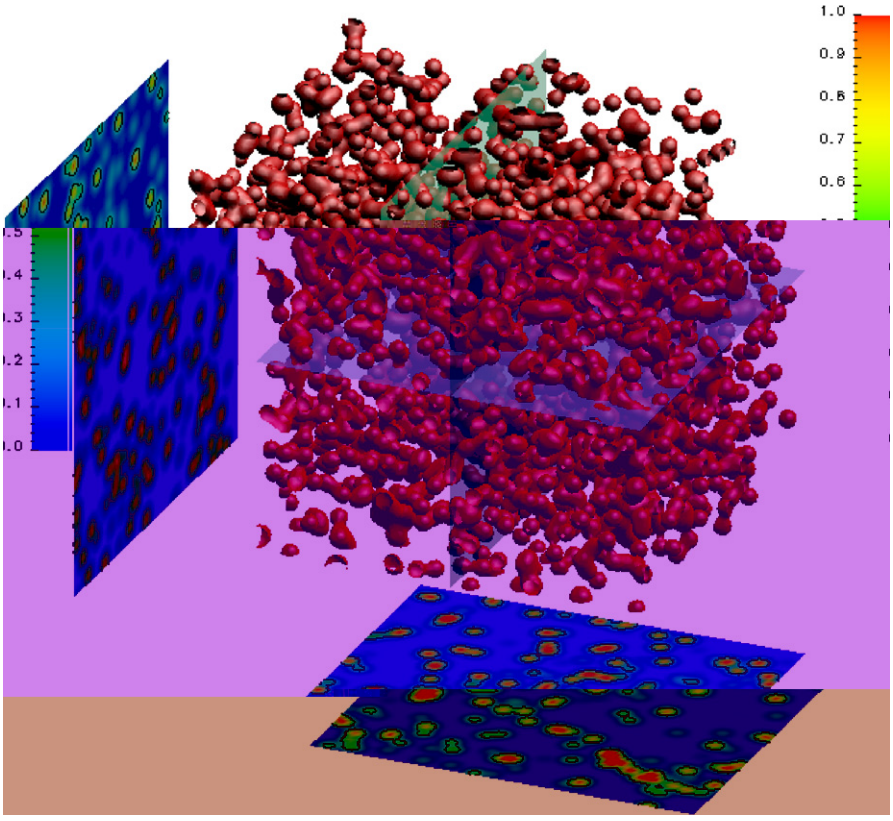

Fig. 6. Initial state of a numerical simulation with 2500 cells/mm^3. The colorbar on the right is referred to the coloring of the cross sections. The red three-dimensional isosurface corresponds to the black contour lines in the cross sections ($t = 0$).

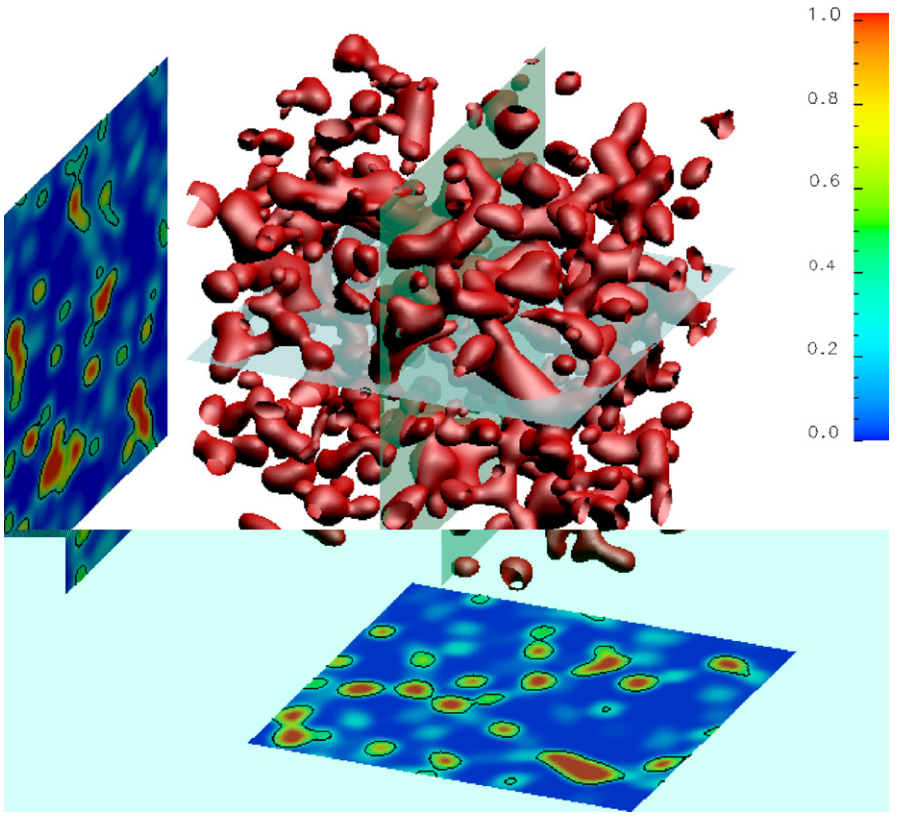

Fig. 7. Transient state of the evolution of the initial state depicted in Fig. 6 according to model (1). The initial formation of network-like structures is observed ($t = 40$).

the stationary state depend on $\bar{n}$ and we observed a percolative phase transition similar to the one described in [10] for the two-dimensional case.

5.1. Analysis of the percolative phase transition

In experimental blood vessel formation it has been shown that a percolative transition is observed, by varying the initial cell density [10]. For low cell densities only isolated clusters of endothelial cells are observed, while for very high densities cells fill the whole available space. In between these two extreme behaviours, close to a critical cell density n_c, one observes the formation of critical percolating clusters connecting opposite sides of the domain, characterized by well defined scaling laws and exponents. These exponents are known not to depend on the microscopic details of the process while their values characterize different classes of aggregation dynamics [27,10].

The purely geometric problem of percolation is actually one of the simplest phase transitions occurring in nature. Many percolative models show a second order phase transition at a critical value n_c of the average density $\bar{n}$, *i.e.* the probability Π of observing an infinite, percolating cluster is 0 for $\bar{n} < n_c$ and *1* for $\bar{n} > n_c$ [27]. The phase transition can be studied by focusing on the values of an order parameter, i.e. an observable quantity that is zero before the transition and takes on values of order 1 after it. In a percolation problem the natural order parameter is the probability P that a randomly chosen site belongs to the infinite cluster (on finite grids, the infinite cluster is substituted by the largest one).

In the vicinity of the critical density n_c the geometric properties of clusters show a peculiar scaling behavior. For instance, in a system of linear finite size L, the probability of percolation $\Pi(n, L)$, defined empirically as the fraction of computational experiments that produce a percolating cluster, is actually a function of the combination $(n - n_c)\, L^{1/\nu}$, where ν is a universal exponent [27].

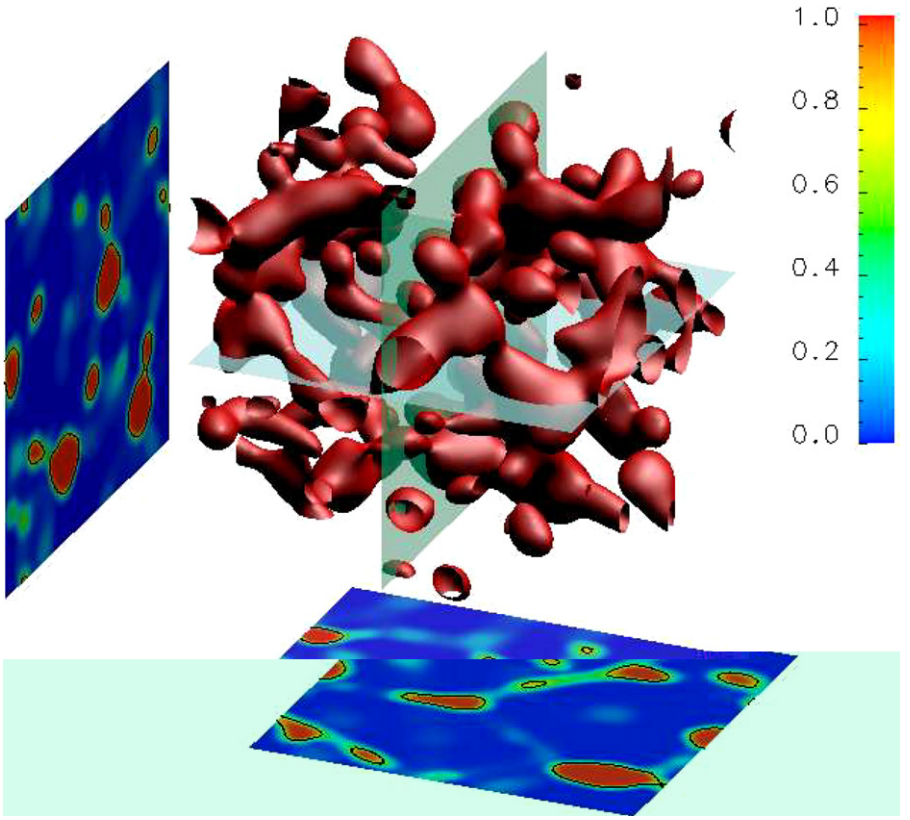

Fig. 8. Stationary state of the evolution of the states depicted in Figs. 6 and 7 according to model (1). Well developed three-dimensional network-like structures are observed ($t = 60$).

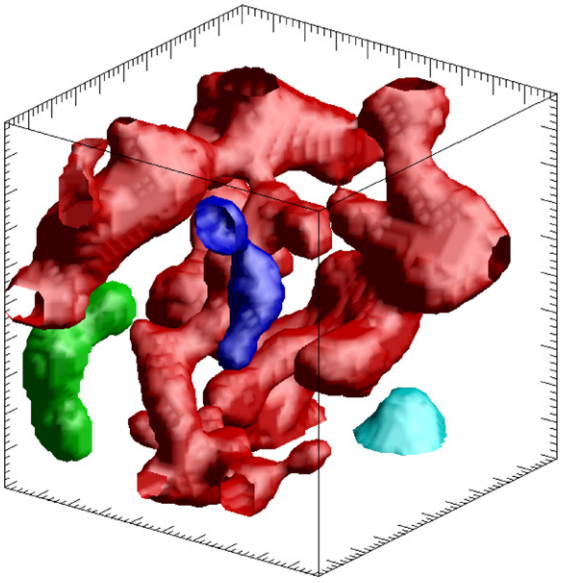

Fig. 9. Cluster percolation with cell density $n = 2500$ cells/mm^3. We show some connected clusters in a realization of model (1). The largest cluster shown in red is a percolating cluster.

In a neighborhood of the critical point and on a system of finite size L, the following finite size scaling relations is also observed:

$$\Pi(\bar{n}, L) \sim \widehat{\Pi}[(\bar{n} - n_c)L^{1/\nu}] \tag{14}$$

There are two main reasons to study percolation in relation to vascular network formation: (i) percolation is a fundamental property for vascular networks, since blood should have the possibility to travel across the whole vascular network to carry nutrients to tissues; (ii) critical exponents are robust observables characterizing the aggregation dynamics.

A rather complete characterization of percolative exponents in the two-dimensional case has been provided in [10].

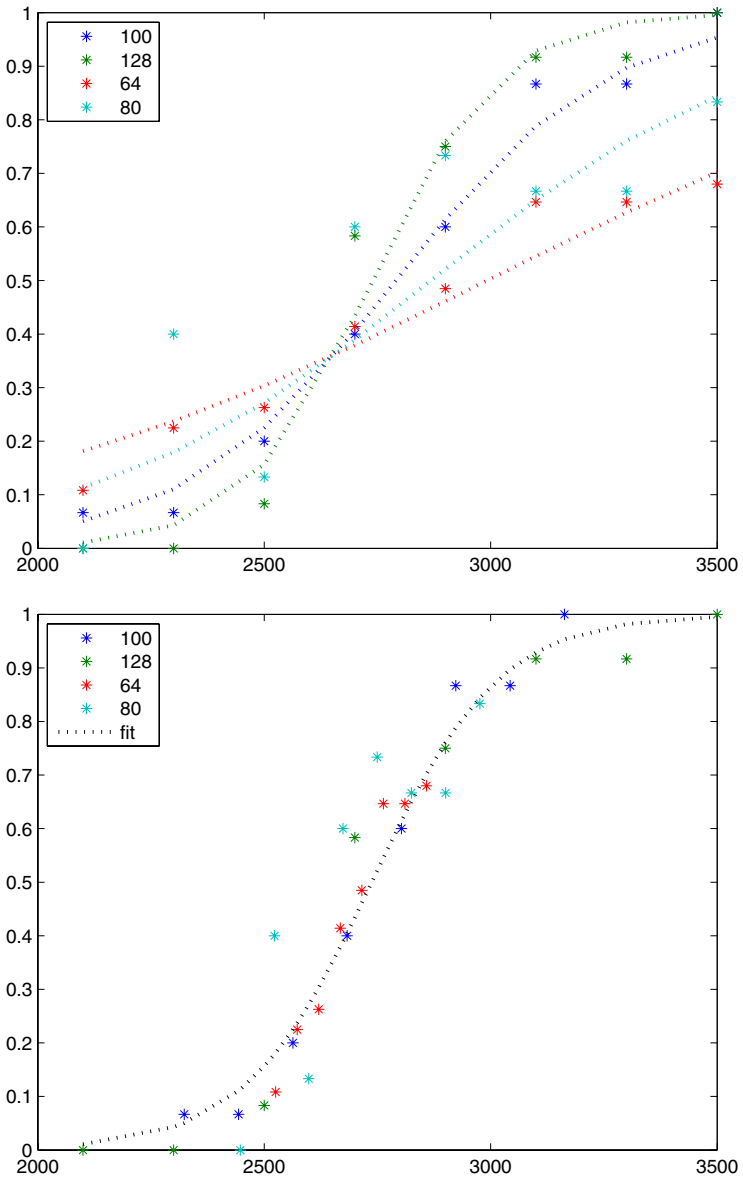

Fig. 10. Percolation probability at varying densities and system sizes (top). After using formula (14), the data collapse (bottom).

As a first step in the study of the more realistic three-dimensional case, we compute the exponent ν characterizing the structures produced by the model dynamics (1) with varying initial cell density.

To this aim, extensive numerical simulation of system (1) were performed using lattice sizes $L = 1, 0.78, 0.62, 0.5$ mm, with different values of the initial density $\bar{n}$. For each point 10–15 realizations of the system of size 1 mm were computed, depending on the proximity to the critical point.

The continuous density at final time $n(\mathbf{x})$ was then mapped to a set of occupied and empty sites by choosing a threshold n_0. Each region of adjacent occupied sites (cluster) was marked with a different index. The percolation probability Π for each set of realizations was then measured. In Fig. 9 we show clusters obtained in a box with $L = 0.5$ mm with $\bar{n} = 3100$. The largest percolating cluster is shown in red, together with some other smaller clusters shown in different colors.

Using relation (14), we estimate the position of the critical point n_c and the value of the critical exponent ν. The data for different box side length and initial density should lie on a single curve after rescaling the densities as $\hat{n} = (\bar{n} - n_c)L^{1/\nu}$. For fixed n_c and ν we rescale $\bar{n}$ and fit the data with a logistic curve, then compute the distance of the data from the curve. The squared distance is minimized to obtain estimates for n_c and ν.

Using $n_0 = 0.35$ we obtain $n_c = 2658$ and $\nu = 0.84$ (the data collapse in shown in Fig. 10). This latter value is compatible with the known value 0.88 for random percolation in three dimensions [27].

6. Conclusions

Understanding the dynamical process of vascularization is an important challenge for contemporary biology, which has clinical implications, like the possibility of testing medical treatments *in silico*. Recent biological research suggests that morphogenetic processes should be studied in their intrinsic three-dimensional setting, where peculiar effects are observable, which are lost in lower dimensional models. Progress in visualization and experimental techniques is on the other hand making possible to get real three-dimensional data of this process.

Taking into account directed cell motility and an autocrine loop of chemoattractant signalling, a differential model can be formulated. It is relevant to check whether this model is able to reproduce the main features of the natural process. This requires the implementation of an efficient numerical scheme to integrate a genuinely three-dimensional mixed system consisting of a reaction-diffusion equation coupled with hyperbolic balance laws. We showed that this difficult numerical task can be effectively implemented by using a novel coupling of relaxed schemes with difference methods for diffusion operators. Moreover we provide a TVD stability analysis for the numerical fluxes in the one-dimensional setting. Our results provide a satisfactory validation of the theoretical model in that percolating network-like structures similar to those observed experimentally are reproduced. It is worth observing here that percolation is a non-trivial property of a blood vessel network, fundamental for its proper functioning.

As a starting point towards a quantitative comparison between experimental data and the theoretical model we need to select a set of observables which provide robust quantitative information on the network geometry. The lesson learned from the study of two-dimensional vasculogenesis is that percolative exponents are an interesting set of such observables, so we tested the computation of percolative exponents on simulated network structures.

We are working on a more thorough comparison of the geometrical properties of experimental and computational network structures, which will become possible as soon as an adequate amount of experimental data will be available, allowing proper statistical computation.

References

[1] A. Abbott, Cell culture: biology's new dimension, Nature 424 (6951) (2003) 870–872.
[2] A.J. Koch, H. Meinhardt, Biological pattern formation: from basic mechanisms to complex structures, Rev. Mod. Phys. 66 (1481–1510) (1994).
[3] D. Ambrosi, A. Gamba, G. Serini, Cell directional persistence and chemotaxis in vascular morphogenesis, Bull. Math. Biol. 66 (6) (2004) 1851–1873.
[4] U. Asher, S. Ruuth, R.J. Spiteri, Implicit–explicit Runge–Kutta methods for time dependent partial differential equations, Appl. Numer. Math. 25 (1997) 151–167.

[5] J. Burgers, The Non Linear Diffusion Equation, D. Reidel Publ. Co., 1974.
[6] P. Carmeliet, Mechanisms of angiogenesis and arteriogenesis, Nat. Med. 6 (2000) 389–395.
[7] E. Cukierman, R. Pankov, D.R. Stevens, K.M. Yamada, Taking cell–matrix adhesions to the third dimension, Science 294 (5547) (2001) 1708–1712.
[8] S. Di Talia, A. Gamba, F. Lamberti, G. Serini, Role of repulsing factors in vascularization dynamics, Phys. Rev. E 73 (2006) 041917-1–041917-11.
[9] P. Friedl, Dynamic imaging of the immune system, Curr. Opin. Immunol. 16 (4) (2004) 389–393.
[10] A. Gamba, D. Ambrosi, A. Coniglio, A. de Candia, S. Di Talia, E. Giraudo, G. Serini, L. Preziosi, F. Bussolino, Percolation, morphogenesis, and Burgers dynamics in blood vessels formation, Phys. Rev. Lett. 90 (2003) 118101.
[11] A.C. Guyton, J.E. Hall, Textbook of Medical Physiology, W.B. Saunders, St. Louis, 2000.
[12] Ami Harten, On a class of high resolution total-variation-stable finite difference schemes, SIAM J. Numer. Anal. 21 (1) (1984) 1–23.
[13] S. Jin, Z. Xin, The relaxation schemes for systems of conservation laws in arbitrary space dimension, Commun. Pure Appl. Math. 48 (1995) 235–276.
[14] Shi Jin, Lorenzo Pareschi, Giuseppe Toscani, Diffusive relaxation schemes for multiscale discrete-velocity kinetic equations, SIAM J. Numer. Anal. 35 (6) (1998) 2405–2439.
[15] M. Kardar, G. Parisi, Y.C. Zhang, Dynamical scaling of growing interfaces, Phys. Rev. Lett. 56 (1986) 889–892.
[16] Christopher A. Kennedy, Mark H. Carpenter, Additive Runge–Kutta schemes for convection–diffusion-reaction equations, Appl. Numer. Math. 44 (1-2) (2003) 139–181.
[17] R.J. LeVeque, Numerical Methods for Conservation Laws, Birkhauser, Zurich, 1990.
[18] B.B. Mandelbrot, Fractal Geometry of Nature, Freeman and Co., San Francisco, 1988.
[19] G. Naldi, L. Pareschi, Numerical schemes for hyperbolic systems of conservation laws with stiff diffusive relaxation, SIAM J. Numer. Anal. 37 (2000) 1246–1270.
[20] L. Pareschi, G. Russo, Implicit–explicit Runge–Kutta schemes and applications to hyperbolic systems with relaxation, J. Sci. Comput. 25 (2005) 129–155.
[21] P.J. Keller, F. Pampaloni, E.H.K. Stelzer, Life sciences require the third dimension, Curr. Opin. Cell Biol. 18 (2006) 117–124.
[22] Alain Pluen, Paolo A. Netti, Rakesh K. Jain, David A. Berk, Diffusion of macromolecules in agarose gels: comparison of linear and globular configurations, Biophys. J. 77 (1999) 542–552.
[23] G. Serini, D. Ambrosi, E. Giraudo, A. Gamba, L. Preziosi, F. Bussolino, Modeling the early stages of vascular network assembly, EMBO J. 22 (2003) 1771–1779.
[24] S.F. Shandarin, Ya.B. Zeldovich, The large-scale structure of the universe: turbulence, intermittency, structures in a self-gravitating medium, Rev. Mod. Phys. 61 (1989) 185–220.
[25] C. Shu, Essentially non-oscillatory and weighted essentially non-oscillatory schemes for hyperbolic conservation laws, in: Advanced Numerical Approximation of Nonlinear Hyperbolic Equations (Cetraro, 1997), Lecture Notes in Math, vol. 1697, Springer, Berlin, 1998, pp. 325–432.
[26] H.E. Stanley, Introduction to Phase Transitions and Critical Phenomena, Oxford University Press, 1987.
[27] D. Stauffer, A. Aharony, Introduction to Percolation Theory, Taylor & Francis, London, 1994.
[28] G.B. West, J.H. Brown, B.J. Enquist, A general model for the origin of allometric scaling laws in biology, Science 276 (5309) (1997) 122–126.
[29] G.B. West, J.H. Brown, B.J. Enquist, The fourth dimension of life: fractal geometry and allometric scaling of organisms, Science 284 (5420) (1999) 1677–1679.